Closely packed, low reorganization energy π-extended postfullerene acceptors for efficient polymer solar cells

Steven M. Swick[a,b,1], Weigang Zhu[a,b,1], Micaela Matta[a,b], Thomas J. Aldrich[a,b], Alexandra Harbuzaru[c], J. Teodomiro Lopez Navarrete[c], Rocio Ponce Ortiz[c], Kevin L. Kohlstedt[a,b,2], George C. Schatz[a,b,2], Antonio Facchetti[a,b,d,2], Ferdinand S. Melkonyan[a,b,2], and Tobin J. Marks[a,b,e,2]

[a]Department of Chemistry, Northwestern University, Evanston, IL 60208; [b]Argonne–Northwestern Solar Energy Research Center, Northwestern University, Evanston, IL 60208; [c]Department of Physical Chemistry, University of Málaga, 29071 Malaga, Spain; [d]Flexterra Corporation, Skokie, IL 60077; and [e]Department of Materials Science and Engineering, Northwestern University, Evanston, IL 60208

Contributed by Tobin J. Marks, July 25, 2018 (sent for review May 17, 2018; reviewed by Jenny Nelson and Colin Nuckolls)

New organic semiconductors are essential for developing inexpensive, high-efficiency, solution-processable polymer solar cells (PSCs). PSC photoactive layers are typically fabricated by film-casting a donor polymer and a fullerene acceptor blend, with ensuing solvent evaporation and phase separation creating discrete conduits for photogenerated holes and electrons. Until recently, n-type fullerene acceptors dominated the PSC literature; however, indacenodithienothiophene (IDTT)-based acceptors have recently enabled remarkable PSC performance metrics, for reasons that are not entirely obvious. We report two isomeric IDTT-based acceptors 3,9-bis(2-methylene-(3-(1,1-dicyanomethylene)-benz-(5,6)indanone))-5,5,11,11-tetrakis(4-nonylphenyl)-dithieno[2,3-d:2′,3′-d′]-s-indaceno[1,2-b:5,6-b′]di-thiophene (ITN-C9) and 3,9-bis(2-methylene-(3-(1,1-dicyanomethylene)-benz(6,7)indanone))-5,5,11,11-tetrakis (4-nonylphenyl)-dithieno[2,3-d:2′,3′-d′]-s-indaceno[1,2-b:5,6-b′]dithiophene (ITzN-C9) that shed light on the exceptional IDTT properties vis-à-vis fullerenes. The neat acceptors and blends with fluoropolymer donor poly{[4,8-bis[5-(2- ethylhexyl)-4-fluoro-2-thienyl]benzo[1,2-b:4,5-b′]dithiophene2,6-diyl]-*alt*-[2,5-thiophenediyl[5,7-bis(2-ethylhexyl)-4,8-dioxo4H,8H-benzo[1,2-c:4,5-c′]dithiophene-1,3-diyl]]} (PBDB-TF) are investigated by optical spectroscopy, cyclic voltammetry, thermogravimetric analysis, differential scanning calorimetry, single-crystal X-ray diffraction, photovoltaic response, space-charge-limited current transport, atomic force microscopy, grazing incidence wide-angle X-ray scattering, and density functional theory-level quantum chemical analysis. The data reveal that ITN-C9 and ITzN-C9 organize such that the lowest unoccupied molecular orbital-rich end groups have intermolecular π−π distances as close as 3.31(1) Å, with electronic coupling integrals as large as 38 meV, and internal reorganization energies as small as 0.133 eV, comparable to or superior to those in fullerenes. ITN-C9 and ITzN-C9 have broad solar-relevant optical absorption, and, when blended with PBDB-TF, afford devices with power conversion efficiencies near 10%. Performance differences between ITN-C9 and ITzN-C9 are understandable in terms of molecular and electronic structure distinctions via the influences on molecular packing and orientation with respect to the electrode.

solar energy | organic photovoltaic | small molecule acceptor | single crystal | molecular modeling

Organic semiconductor technologies have witnessed rapid recent advances and are being incorporated in increasing numbers of optoelectronic products (1). In addition to rivaling the performance of many inorganic materials, organics offer the attraction of low-cost solution processing to fabricate large-area, flexible, lightweight panels (2, 3). For polymer solar cells (PSCs), great strides have been made in performance, with power conversion efficiencies (PCEs) now exceeding 13% (4–7). PSC photoactive layers are commonly created by film-casting bulk heterojunction (BHJ) blends of p-type donor polymers and n-type fullerene acceptors (Fig. 1*B*), with the ensuing solvent evaporation and phase separation creating discrete conduits for photogenerated hole and electron conduction to the cell electrodes for collection. It has long been conjectured that fullerenes, with their spherical shapes that afford close packing, orbital degeneracies, and low internal charge-transfer reorganization energies, are uniquely suited for the n-type acceptor role (8, 9). In optimum cases, fullerene BHJ devices have produced PCEs >10% (10, 11). Nevertheless, fullerene acceptors are limited in optical cross-section (Fig. 1*C*) as well as environmental and phase stability (12). To address these limitations, substantial research has been devoted to investigating novel, nonfullerene acceptors (13–16) including those derived from rylene diimides (17–19) and diketopyrrolopyrroles (20).

However, a new class of PSC n-type molecular acceptors based on the indacenodithienothiophene (IDTT) skeleton has emerged (Fig. 1*A*). Interestingly, IDTT acceptors appear to be remarkably different from fullerenes in the aforementioned key properties thought necessary for efficient BHJ n-type acceptor performance (12, 21). Nevertheless, some IDTT acceptors deliver PCEs exceeding

Significance

For producing electricity, polymer solar cells (PSCs) offer properties tunability, light weight, scalability, and earth-abundant materials. PSC active layers typically consist of donor polymer and fullerene acceptor blends having discrete conduits for photogenerated hole and electron conduction. The spherical fullerene shape, which enables close packing, orbital degeneracies, and low charge-transfer reorganization energies, is thought to be essential for efficient photocurrent generation and high power conversion efficiencies (PCEs). However, the recent advent of irregularly shaped indacenodithienothiophene (IDTT) acceptors yielding higher PCEs challenges the fullerene paradigm. In a combined experimental and theoretical study with two new isomeric IDTT derivatives, we shed light on the basis of this performance in terms of surprisingly close molecular packing, strong electronic coupling, and low reorganization energies.

Author contributions: K.L.K., G.C.S., A.F., F.S.M., and T.J.M. designed research; S.M.S., W.Z., M.M., T.J.A., A.H., J.T.L.N., and R.P.O. performed research; S.M.S., W.Z., M.M., T.J.A., K.L.K., G.C.S., A.F., F.S.M., and T.J.M. analyzed data; and S.M.S., W.Z., M.M., T.J.A., K.L.K., G.C.S., A.F., F.S.M., and T.J.M. wrote the paper.

Reviewers: J.N., Imperial College London; and C.N., Columbia University.

The authors declare no conflict of interest.

Data deposition: Crystallography, atomic coordinates, and structure factors reported in this paper have been deposited in the Cambridge Structural Database, Cambridge Crystallographic Data Centre, www.ccdc.cam.ac.uk (accession nos. 1817196 and 1817197).

[1]S.M.S. and W.Z. contributed equally to this work.

[2]To whom correspondence may be addressed. Email: kkohlstedt@northwestern.edu, g-schatz@northwestern.edu, a-facchetti@northwestern.edu, f-melkonyan@northwestern.edu, or t-marks@northwestern.edu.

This article contains supporting information online at www.pnas.org/lookup/suppl/doi:10.1073/pnas.1807535115/-/DCSupplemental.

Published online August 20, 2018.

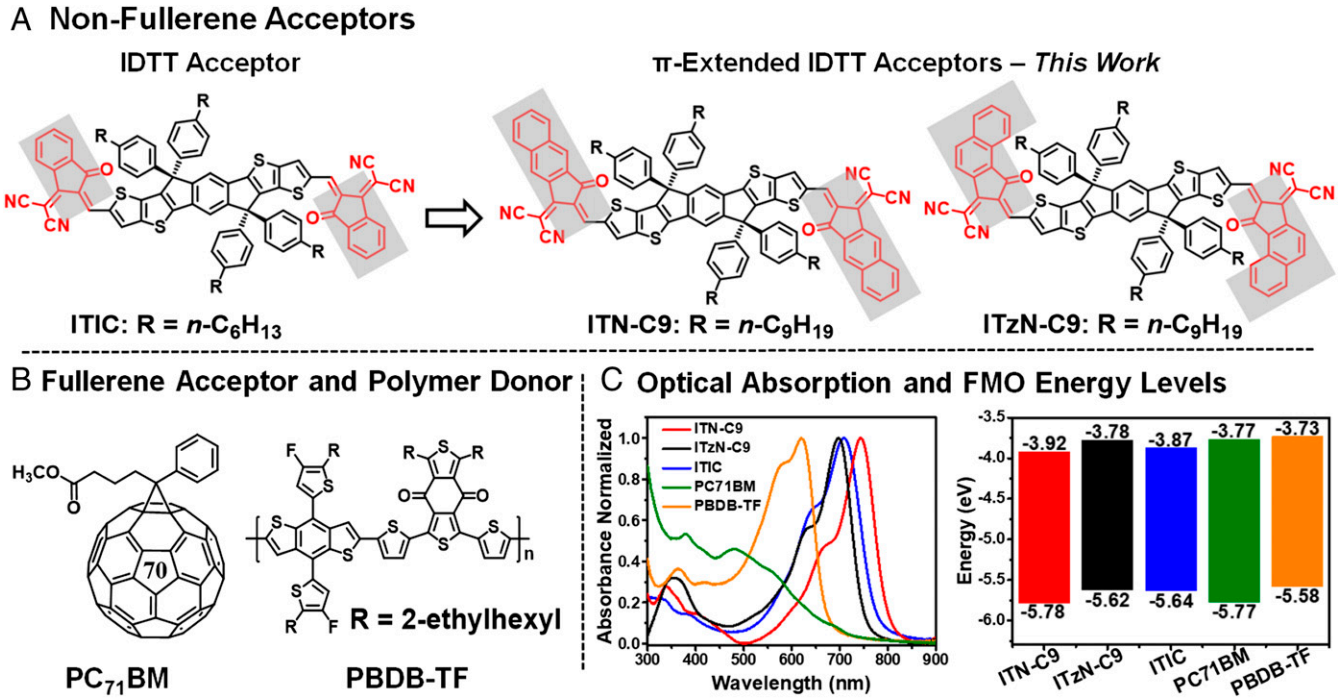

Fig. 1. Chemical structures of (*A*) typical IDTT acceptor (**ITIC**) and π-extended IDTT acceptors (**ITN-C9** and **ITzN-C9**) and (*B*) C_{70} fullerene acceptor derivative and donor polymer **PBDB-TF**. (*C*) Comparative thin film optical absorption spectra and CV-derived FMO energies of **ITN-C9**, **ITzN-C9**, **ITIC**, **$PC_{71}BM$** (57), and **PBDB-TF**.

13% in blends with well-known donor polymers (6). The reasons underlying this exceptional performance are not obvious, raise questions about current paradigms used to design BHJ PSCs, and reflect a lack of information as basic as the IDTT molecular organization patterns involved.

Here we report the realization of a class of π-extended IDTT derivatives, **IT(z)N-CX** (Fig. 1*A*), and their detailed characterization alone and in blends with the donor fluoropolymer **PBDB-TF** (Fig. 1*B*) (22), which is known to yield high-performance devices with nonfullerene acceptors (23, 24). Theoretical studies argue that extended π-conjugation enhance intermolecular π–π binding energies (25), and, in polyacenes, affords lower internal reorganization energies due to delocalization of the charge-induced polarization density (26, 27). Clearly, detailed analysis of π-extended IDTT derivatives, if realized, should contribute to the fundamental understanding of this new class of n-type materials and identify directions for further advances. The battery of physicochemical techniques applied here to the neat acceptors and their blends includes optical spectroscopy, cyclic voltammetry (CV), thermogravimetric analysis (TGA), differential scanning calorimetry (DSC), single-crystal X-ray diffraction, photovoltaic (PV) response, space-charge-limited current (SCLC) transport, atomic force microscopy (AFM), and grazing incidence wide-angle X-ray scattering (GIWAXS), as well as density functional theory (DFT)- and Zerner's Intermediate Neglect of Differential Overlap (ZINDO/S)-level quantum chemical analysis. The results show that, in the solid phase, the IDTT acceptors **ITN** and **ITzN** form columns of face-to-face packed molecules, with close π–π interactions between the lowest unoccupied molecular orbital (LUMO)-rich electron-deficient naphthyl end groups, implying that electron transport proceeds primarily through these fragments. In addition, the IDTT acceptors reported here are shown to have smaller internal reorganization energies, comparable intermolecular π–π electronic coupling integrals, and electron mobilities approaching those of fullerene acceptors.

Results and Discussion

Molecular Design and Characterization of π-Extended IDTT Acceptors. To increase IDTT π-delocalization, two isomeric structures in which phenylene moieties fused to the electron-deficient end groups were designed. For organic semiconductors in general and IDTT-based acceptors, thin film structural/physicochemical properties and PV performance are sensitive to the shape and length of solubilizing alkyl substituents attached to the molecular/macromolecular core (28, 29). Thus, we first synthesized three derivatives of the linearly extended **ITN** acceptor with progressively elongated alkyl chains: **ITN-C6** (R = *n*-C_6H_{13}), **ITN-C9** (R = *n*-C_9H_{19}), and **ITN-C12** (R = *n*-$C_{12}H_{25}$) (Fig. 1*A*). See *Materials and Methods* for synthetic and characterization details. Due to the tendency of **ITN-C6** to phase separate as large crystals in blends with **PBDB-TF**, extremely low PV response was measured for this acceptor (see *PV and Charge Transport Measurements*). However, preliminary organic PV (OPV) evaluation utilizing **ITN-C9** or **ITN-C12** as acceptors yielded good PCEs, with the R = *n*-nonyl (*n*-C_9H_{19}) side chain proving optimal. Thus, for the isomeric, zigzag extended **ITzN** acceptor, the *n*-nonyl (*n*-C_9H_{19}) side chain was selected for further studies. With these acceptors in hand, systematic optical and electrochemical characterization was carried out; data are summarized in Table 1.

All **ITN-CX** acceptors exhibit identical optical absorption profiles in solution with λ_{max} centered at ~710 nm (*SI Appendix*, Fig. S1). Interestingly, compared with **ITN-CX**, the **ITzN-C9** λ_{max} is significantly blue-shifted (~667 nm), indicating significant electronic structure differences. In thin films, all **ITN-CX** acceptors exhibit similar absorption profiles, which are red-shifted versus those in solution (Fig. 1*C* and *SI Appendix*, Fig. S1). Similarly, the **ITzN-C9** film λ_{max} is red-shifted versus that in solution. The absorption edge was also used to estimate optical bandgaps (E_g^{OPT}), revealing that **ITN-CXs** have smaller bandgaps than **ITzN-C9** (Table 1). Interestingly, in comparison with **ITIC** (3,9-bis(2-methylene-(3-(1,1-dicyanomethylene)-indanone))-5,5,11,11-tetrakis(4-hexylphenyl)-dithieno[2,3-d:2′,3′-d′]-s-indaceno[1,2-b:5,6-b′]dithiophene),

Table 1. Summary of ITN-CX and ITzN-C9 optical and thermal properties

Compound	λ_{max}, nm		λ_{onset}, nm		E_g^{OPT} Film, eV	T_d,* °C	T_{DSC}, °C
	Solution	Film	Solution	Film			
ITN-C6	709	747	756	817	1.52	378	—
ITN-C9	709	744	756	803	1.54	341	199.5†
ITN-C12	709	735	756	795	1.56	342	—
ITzN-C9	667	698	719	751	1.65	350	200.5† 226.0;193.0‡

Solution optical spectra were measured in 0.0100 mg/mL $CHCl_3$ solutions. Film optical spectra were measured on films cast from 5.0 mg/mL $CHCl_3$ solutions on glass slides; optical gap (E_g^{OPT}) was estimated from the absorption edge.

*TGA samples heated at 10 °C/min under an N_2 atmosphere, with T_d defined as temperature of 5% mass loss.

†Cold crystallization temperature (observed only in the first DSC heating cycle).

‡Melting and crystallization temperatures, respectively (DSC second cycle).

ITN-CXs have red-shifted optical absorption, whereas **ITzN-C9** exhibits blue-shifted absorption as both solutions and thin films. Overall, **ITN-CX**s and **ITzN-C9** strongly absorb at ~650 nm to 800 nm and ~600 nm to 720 nm, respectively, which should be attractive for efficient solar light capture if paired with a medium-large bandgap donor semiconductor such as **PBDB-TF**. Thin-film CV experiments were next used to assess the redox properties and thus the highest occupied molecular orbital (HOMO) and LUMO energetics of the **ITN-CX** series and **ITzN-C9**. **ITN-CXs** and **ITzN-C9** exhibit quasi-reversible oxidation and irreversible reduction waves (*SI Appendix*, Fig. S2 and Table S2). Interestingly, **ITzN-C9** and **ITN-C6** have similar HOMO energies, while **ITN-C9** and **ITN-C12** possess lower-lying HOMOs. All **ITN-CX** molecules have similar LUMO energies, in contrast to **ITzN-C9**, which has an elevated LUMO (Fig. 1*C*). Overall, **ITN-CX**s and **ITzN-C9** have energy levels that are perturbed from **ITIC** but show good alignment with **PBDB-TF**. Next, the thermal

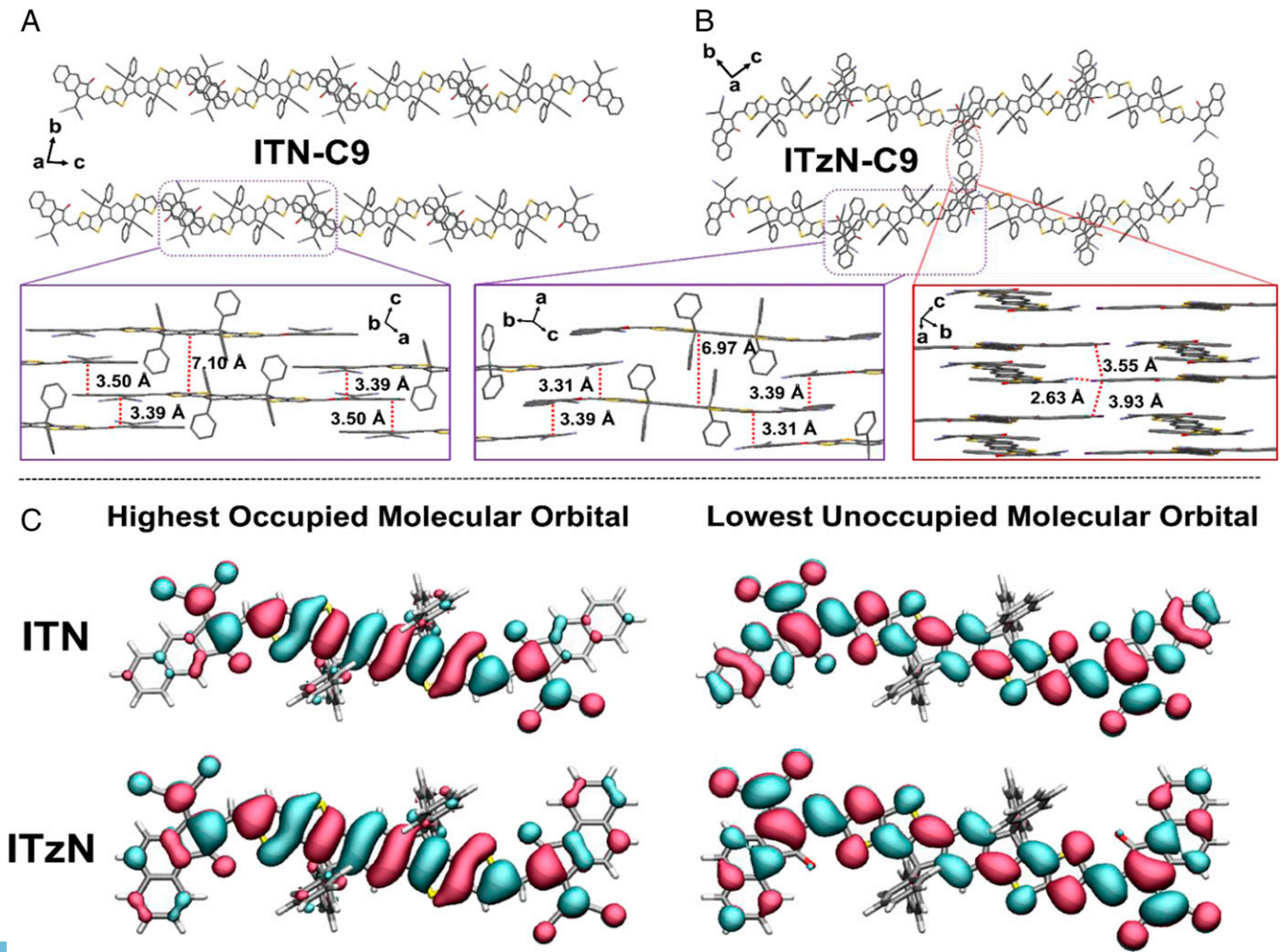

Fig. 2. Crystal packing of (*A*) **ITN-C9** and (*B*) **ITzN-C9** with the closest π–π contacts shown. (*C*) Computed HOMO and LUMO contours of **ITN** and **ITzN**.

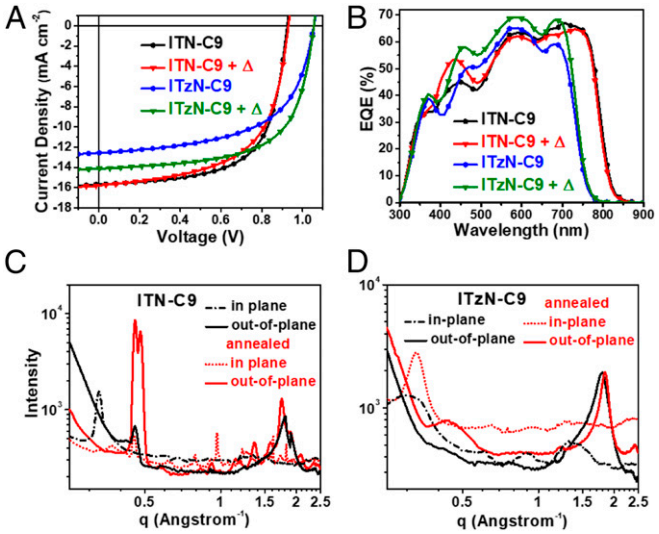

Fig. 3. **PBDB-TF:IT(z)N-C9** PSCs: (*A*) *J*–*V* responses and (*B*) EQE spectra. Δ indicates annealing. Neat film GIWAXS linecuts of (*C*) **ITN-C9** and (*D*) **ITzN-C9**.

properties of the **ITN-CX**s and **ITzN-C9** were investigated using TGA and DSC (Table 1). All series members exhibit high thermal decomposition temperatures (T_d) of >340 °C (5% mass loss; Table 1 and *SI Appendix*, Fig. S4). DSC data are of interest because previous studies showed that annealing BHJ blends at the acceptor cold crystallization temperature can enhance PCE (28). **ITN-C9** and **ITzN-C9** exhibit such cold crystallizations at 199.5 °C and 200.5 °C, respectively, on the first heating cycle, whereas **ITN-C6** and **ITN-C12** show no obvious thermal transitions (*SI Appendix*, Fig. S5). In addition to the cold crystallization, **ITzN-C9** exhibits reversible melting and crystallization at 226.0 °C and 193.0 °C, respectively.

Solid-State Structure and Molecular Orbital Computations. Understanding the solid-state organization of new nonfullerene acceptors is of great importance for the rational design of PSC components, yet there is a striking paucity of single-crystal diffraction data (25). To gain detailed insight into **ITN-C9** and **ITzN-C9** molecular packing, suitable single crystals for diffraction studies were grown, and diffraction data was acquired (see *Materials and Methods* and *SI Appendix*, *SI Materials and Methods* for details). The crystal structures of **ITN-C9** and **ITzN-C9** (Fig. 2 *A* and *B*) indicate that both molecules adopt planar π-systems with intramolecular S···O=C conformation-locking interactions (30, 31). Both molecules pack in triclinic lattices with π-planes stacking along the unit cell *a* axis (*SI Appendix*, Figs. S8 and S10) in "face-to-face" slip-stacked columns. Interestingly, this is in stark contrast to **ITIC**, which exhibits an "edge-to-face" crystal structure (25), possibly reflecting the stronger π–π interactions of the **ITN-C9** and **ITzN-C9** naphthyl end groups favoring a "face-to-face" packing motif. Multiple short intermolecular π–π interactions between the naphthyl groups feature two short distances of 3.39(2) and 3.50(2) Å for **ITN-C9**, and 3.31(1) and 3.39 (1) Å for **ITzN-C9**. Note that the attached phenylalkyl substituents prevent close approach of the IDTT cores which are separated by distances of 7.10(2) and 6.97(1) Å for **ITN-C9** and **ITzN-C9**, respectively, suggesting that electron transport proceeds primarily through the π-stacked naphthyl groups. Interestingly, the **ITzN-C9** angled naphthyls allow additional π–π interactions [3.55 (2) Å, 3.93(1) Å] and short CN···H–Ar hydrogen bonding interactions [2.634 (7) Å, 3.180(8) Å] (32, 33) between stacks of the acceptor, promoting a honeycomb-like network formation, whereas the linearly extended **ITN-C9** end group does not permit interactions between molecular stacks. In comparison with typical fullerene acceptors, the present naphthyl π–π distances are slightly longer than those in crystalline **$PC_{61}BM$** (3.16 Å to 3.19 Å) (34, 35) and **$PC_{71}BM$** (3.15 Å to 3.25 Å) (36, 37).

Computational modeling can provide valuable information for understanding electronic structure and structure–property relationships and, importantly, to define critical variables for rational materials design (38). Here we investigate how naphthyl symmetry affects **ITN** versus **ITzN** optical properties, electronic structure, and frontier molecular orbital (FMO) energies. Computation at the B3LYP/DZP (Becke, 3 parameter, Lee–Yang–Parr, double zeta polarized basis) level indicates that **ITN** has deeper HOMO and LUMO levels (−6.33 and −4.22 eV) than **ITzN** (−6.29 and −4.10 eV) and a smaller band gap (2.11 eV versus 2.19 eV), explaining the experimental optical spectral shifts (*SI Appendix*, Table S4). Since the two molecules are isoelectronic and have similar geometries, the deeper FMOs of **ITN**, particularly the LUMO, are reasonably ascribed to the nodal structure of the **ITN** naphthyl moiety. This may also reflect the lower symmetry, and thus a lower degree of orbital mixing in **ITzN**. The MO nodal features of **ITN** and **ITzN** (Fig. 2*C*) show that the naphthyl moieties contribute significantly to the LUMOs, while the HOMO is primarily confined to the molecular core. This significant naphthyl contribution to the LUMO is of critical significance for the charge transport properties of these acceptors because, as noted above, they assemble with very close naphthyl π–π interactions, whereas the molecular cores are significantly farther apart. Importantly, note that the energy difference between the **ITzN** LUMO and LUMO+1 is smaller (0.21 eV) than in **ITN** (0.29 eV) (*SI Appendix*, Figs. S12 and S13), and that low-lying LUMO+1 orbitals have been linked to better performance for a wide range of small-molecule acceptors, plausibly due to a higher density of charge transfer states in such systems (28, 39).

Charge transport parameters (40, 41) were also compared for **ITN** and **ITzN**. Remarkably, we find that **ITN** and **ITzN** have very low computed internal reorganization energies (λ_{int}s) of 0.133 and 0.147 eV, respectively, and lower than those of **ITIC**

Table 2. **PBDB-TF:IT(z)N and PBDB-TF:$PC_{71}BM$ blend film PSC and SCLC device metrics**

Acceptor	V_{OC}, V	J_{SC}, mA/cm^2	FF, %	PCE, %	$10^4 \times \mu_h$, cm^2·V^{-1}·s^{-1}	$10^4 \times \mu_e$, cm^2·V^{-1}·s^{-1}	μ_h/μ_e
ITN-C6	0.04	2.39	26.2	<0.1 (<0.1 ± 0.01)	—	—	—
ITN-C12	0.93	12.70	56.2	6.61 (6.47 ± 0.09)	—	—	—
ITN-C9	0.92	15.68	64.5	9.33 (8.91 ± 0.23)	2.3 ± 1.1	4.5 ± 2.0	0.50
ITN-C9*	0.93	15.79	59.7	8.76 (8.28 ± 0.47)	3.4 ± 1.2	4.6 ± 3.9	0.73
ITzN-C9	1.06	12.77	58.8	7.99 (7.76 ± 0.21)	2.7 ± 0.5	0.16 ± 0.11	17.5
ITzN-C9*	1.05	14.12	63.9	9.51 (9.17 ± 0.39)	6.3 ± 2.1	3.5 ± 1.7	1.81
$PC_{71}BM$†	0.94	11.52	62.6	6.77 (6.58 ± 0.16)	13.6 ± 6.4	3.6 ± 2.0	3.82

*Annealed at 200 °C for 5 min.
†Annealed at 160 °C for 5 min. V_{OC}, J_{SC}, FF, and PCE are shown for champion cells with averages PCEs (greater than or equal to six devices) in parentheses; SCLC mobilities are averages of greater than or equal to three devices.

(0.155 eV), **$PC_{61}BM$** (0.154 eV), and **$PC_{71}BM$** (0.2 eV) (9, 42, 43). This quantity measures the energetic cost of ionization. Low λ_{int}s values are achieved when the neutral and charged species have very similar geometries, and when the excess charge can be effectively delocalized over the entire molecule, as is the case for both **ITN** and **ITzN**. Since this electrostatic interaction is long-range, there is also an external contribution to the reorganization energy due to the polarization of the medium, but we assume it to be comparable for **ITN** and **ITzN**.

To further quantify the role of π–π stacking and its effect on the **ITN** and **ITzN** band structures, the density of states (DOS) of the two crystals was calculated (*SI Appendix*, Fig. S16). The DOS are computed over all atomic orbitals and then projected onto the molecular basis function so that the lower and upper band edges are the HOMO and LUMO, respectively. The importance of the slip-stacked packing in **ITzN-C9** is evident when analyzing the conduction band DOS, with 69% contributed by the angled naphthyl groups, while, for **ITN-C9**, 52% of the conduction band is provided by the linear naphthyl groups. For comparison, the highest valence band of both acceptors involves the terminal naphthyls by only 27%. The crystal structures of **ITN-C9** and **ITzN-C9** were also used to calculate the electronic coupling (|J|) between nearest-neighbor molecules at the ZINDO level (*SI Appendix*, Fig. S15). The results were then analyzed within the framework of dynamic disorder-dominated charge transport theory (44). **ITN-C9** has six nearest neighbors with nonnegligible transfer integrals, and little or no contribution along the unit cell *b* axis (*SI Appendix*, Table S5). The highest |J| value observed is 5.85 meV, which is relatively low in absolute terms but comparable to the next highest coupling (1.49 meV). The relative magnitude of transfer integrals along different crystallographic axes (and not only their absolute value) correlates with experimental mobilities, with more homogeneous environments leading to higher experimental mobilities and thus better device performance (45). For **ITN-C9** crystalline domains, it appears that electron transport is mostly limited by the absence of coupling along the *b* crystallographic direction. In contrast, **ITzN-C9** exhibits a maximum |J| value of 38.17 meV. Remarkably, the orientation of the four nearest neighbors with the largest couplings (38 and 5 meV; see *SI Appendix*, Table S6) suggests that both greater charge transport dimensionality (42) and higher mobility may be possible in the **ITzN-C9** ordered domains than in **ITN-C9**. Finally, all electronic couplings have the same sign, which is reported (45) to be an important factor in achieving high mobilities. For comparison, **ITIC** has a greatest |J| value of 16 meV (*SI Appendix*, Table S7), crystalline **$PC_{61}BM$** has been reported to have |J| values as high as 50 meV (46, 47), and amorphous **$PC_{61}BM$** and **$PC_{71}BM$** are computed to have average |J|s of ∼12 meV (48). In summary, the combination of low reorganization energies and close π–π stacking of the LUMO-localized terminal naphthyl groups leading to high electronic couplings is encouraging for future studies of **ITN-C9** and, particularly, of **ITzN-C9**, where the electronic coupling distribution suggests a high charge transport dimensionality in crystalline domains. Kinetic Monte Carlo mobility calculations within the framework of Marcus–Jortner theory are planned to assess the exact dimensionality of charge transport (49).

PV and Charge Transport Measurements. The PV efficiency of the new acceptors was next evaluated in BHJ blends with the **PBDB-TF** donor polymer (Fig. 1). First, "inverted architecture" (ITO/ZnO/Active Layer/MoO_3/Ag) PSCs were fabricated using **ITN-CX**s (Fig. 3*A* and Table 2; see *SI Appendix* for details). The **ITN-C6** devices display negligible PV response due to poor film morphology (see *Structural Analysis and PV Response Correlations*), while, impressively, **ITN-C9** and **ITN-C12** PSCs yield average

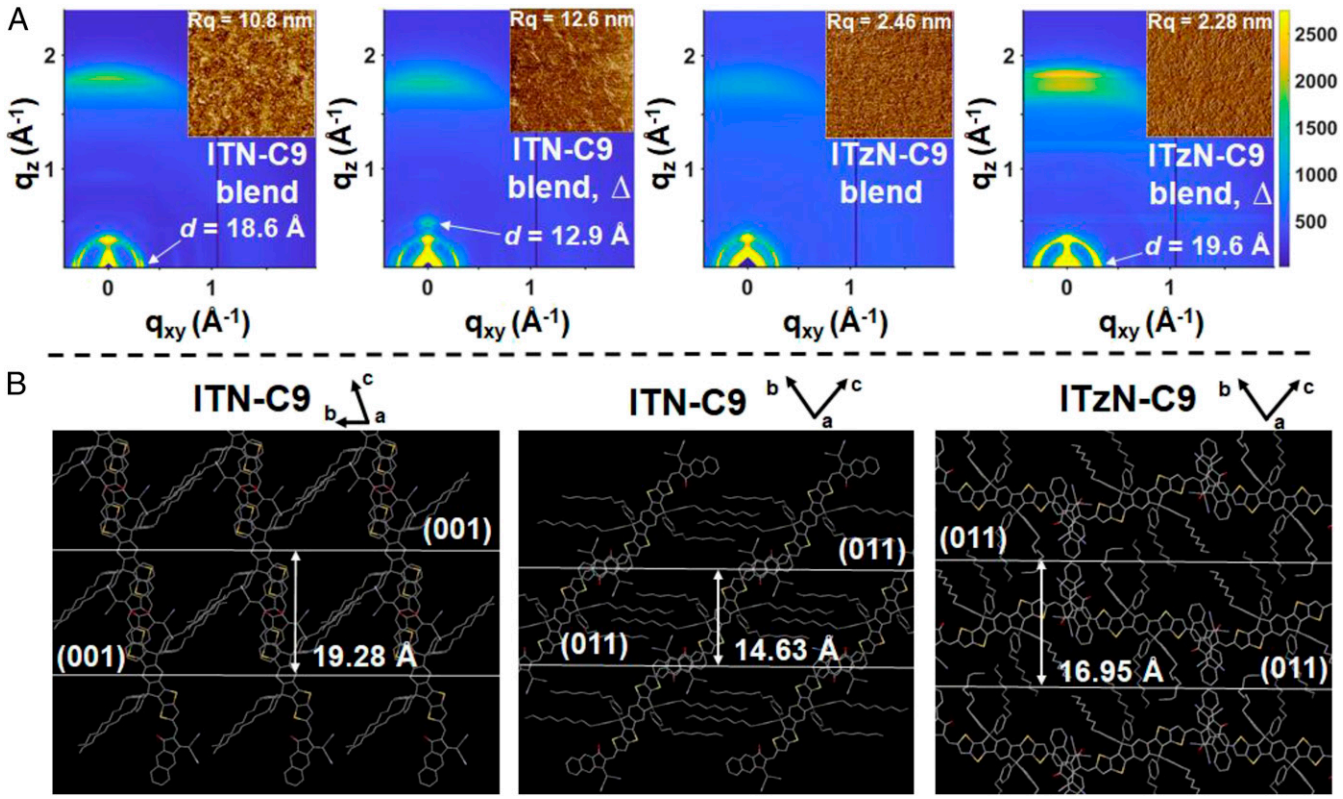

Fig. 4. (*A*) GIWAXS patterns and (*Insets*) AFM phase images (3 × 3 μm) of **PBDB-TF**:**IT(z)N-C9** as-cast and annealed (200 °C for 5 min) films. (*B*) Crystallographic planes relevant to GIWAXS analysis extracted from single crystal structures of **ITN-C9** and **ITzN-C9**.

PCEs of 8.91% (9.33% maximum) and 6.47% (6.61% maximum), respectively. Given the high performance of **ITN-C9**, it was selected for further optimization. Interestingly, annealing the **PBDB-TF**:**ITN-C9** blend films between 80 °C and 250 °C, including the cold crystallization temperature (28), yields lower fill factors (FFs) and, consequently, lower PCEs. In contrast, **ITzN-C9** PSCs exhibit substantial PCE increases (7.99% → 9.51%) on annealing at the cold crystallization temperature (200 °C) with increased J_{SC} and FF. Note that the differing responses of the blends to annealing may reflect film morphology changes triggered by acceptor crystallization and/or different electron transport in ordered **ITN-C9** versus **ITzN-C9** domains. Also note that the **ITzN-C9**–based devices have higher (>1.0 V) open-circuit voltages (V_{OC}s) versus the **ITN**-based PSCs, consistent with the higher-lying **ITzN-C9** LUMO (see *Molecular Design and Characterization of π-Extended IDTT Acceptors*). As a control, analogous **PBDB-TF**:**$PC_{71}BM$** PSCs were fabricated and evaluated. In the "inverted" architecture used here, **PBDB-TF:$PC_{71}BM$** devices deliver average PCEs of 6.58%. PSC metrics are summarized in Table 2.

Note that the **ITzN-C9**–based PSCs exhibit substantial external quantum efficiency (EQE) response over the broad 300-nm to 750-nm range, which increases over the entire range on annealing, whereas **ITN-C9** PSCs show a strong response in the 300-nm to 830-nm range, with increased donor (350 nm to 500 nm) and diminished acceptor (650 nm to 750 nm) response upon annealing (Fig. 3*B*). Overall, the greater **ITN-C9** blend optical absorption range relative to **ITzN-C9** blends is manifest in greater J_{SC} (15.68 versus 14.12 mA/cm^2). Importantly, both current–voltage (*J*–*V*) and EQE data clearly demonstrate the divergent, but complementary, properties of the **ITN-C9** and **ITzN-C9** acceptors. Charge transport properties perpendicular to the substrate plane were next probed using the SCLC model. Single-charge carrier diodes of ITO/MoO_3/Organics/MoO_3/Ag architecture for hole-only and of ITO/ZnO/Organics/LiF/Al for electron-only devices were evaluated, and mobilities were extracted from data in the SCLC regime (see *SI Appendix*, *SI Materials and Methods* for details; *SI Appendix*, Fig. S22). As-cast neat **ITN-C9** and **ITzN-C9** films exhibit electron mobilities (μ_es) of $2.3 \pm 1.3 \times 10^{-4}$ and $2.8 \pm 1.3 \times 10^{-5}$ cm^2·V^{-1}·s^{-1}, respectively (*SI Appendix*, Table S11). Interestingly, while **ITN-C9** annealing affects μ_e only slightly, for **ITzN-C9**, μ_e increases by 10×, yielding μ_es of $6.7 \pm 5.9 \times 10^{-4}$ and $4.4 \pm 2.5 \times 10^{-4}$ cm^2·V^{-1}·s^{-1}, respectively. As noted above, the greater electronic coupling and charge transport dimensionality calculated for **ITzN-C9** crystals versus **ITN-C9** crystals should afford a higher μ_e for **ITzN-C9**. This discrepancy between theoretical and experimental data can be understood by GIWAXS analysis (see *Structural Analysis and PV Response Correlations*), which shows that **ITN-C9** forms much larger crystalline domains than **ITzN-C9** (*SI Appendix*, Table S12), affording fewer grain boundaries and higher mobilities (50). Note that the μ_es observed for neat **ITN-C9** and **ITzN-C9** films are approaching those for fullerenes (10^{-2}–10^{-4} cm^2·V^{-1}·s^{-1}) (51), and are comparable to those for **ITIC** (10^{-4} cm^2·V^{-1}·s^{-1}) (21). As-cast **PBDB-TF** blends with **ITN-C9** and **ITzN-C9** have substantial hole mobilities (μ_hs) of $2.3 \pm 1.1 \times 10^{-4}$ and $2.7 \pm 0.5 \times 10^{-4}$ cm^2·V^{-1}·s^{-1} and μ_es of $4.5 \pm 2.0 \times 10^{-4}$ and $1.6 \pm 1.1 \times 10^{-5}$ cm^2·V^{-1}·s^{-1}, respectively (Table 2). Importantly, for **PBDB-TF**:**ITN-C9** films, balanced mobilities are observed ($\mu_h/\mu_e = 0.50$), with both μ_h and μ_e remaining largely unaffected by annealing, whereas **ITzN-C9** blend films exhibit more than 10× increase in μ_e after annealing, resulting in near-balanced mobilities ($\mu_h/\mu_e = 17.5 \rightarrow 1.81$; Table 2), and consistent with the PCE and multidimensional electron transport in ordered **ITzN-C9** domains discussed above.

Structural Analysis and PV Response Correlations. The thin-film morphologies of neat and blend films were analyzed by AFM and GIWAXS. AFM images of the **PBDB-TF**:**ITN-C6** blends reveal very rough surfaces with an RMS roughness of 119 nm, consistent with the marginal PSC performance (*SI Appendix*, Fig. S17). In contrast, the **PBDB-TF**:**ITN-C9** and **PBDB-TF**:**ITzN-C9** films have smoother surfaces (Fig. 4*A*) that are largely unaffected by annealing. Interestingly, the **PBDB-TF**:**ITN-C9** phase images evolve from a granular as-cast to fibrous annealed morphology (Fig. 4*A* and *SI Appendix*, Fig. S19). In contrast, the surfaces of the **PBDB-TF**:**ITzN-C9** blends have a fibrous morphology and are less affected by thermal treatment. GIWAXS experiments provide key information on materials packing and order in thin films and are typically the only experimental technique to provide this information. In the present case, the single-crystal diffraction data discussed above aid in unambiguously assigning the GIWAXS patterns. Thus, the powder X-ray diffraction (PXRD) patterns of **ITN-C9** and **ITzN-C9** (*SI Appendix*, Figs. S7 and S9) were calculated from the single-crystal diffraction data, and the resulting crystallographic planes (hkl) and interplanar distances (d_{hkl}) were analyzed and compared with the distances (*d*) measured from the GIWAXS experiments. Two major PXRD reflections for **ITN-C9** films correspond to the (001) (d_{001} = 19.28 Å) and the (011) (d_{011} = 14.63 Å) crystallographic planes (Fig. 4*B*). For **ITzN-C9**, three major PXRD reflections correspond to the (001) (d_{001} = 25.07 Å), (010) (d_{010} = 25.07 Å), and (011) (d_{011} = 16.95 Å) planes. All neat materials (as-cast and annealed) were analyzed by GIWAXS to aid in blend film peak assignments

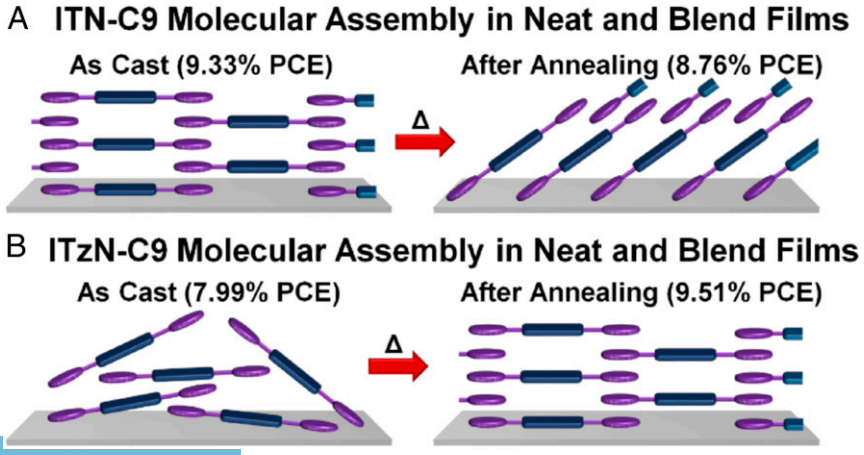

Fig. 5. Schematic representation of the morphological changes observed with annealing neat and **PBDB-TF** blend films of (*A*) **ITN-C9** and (*B*) **ITzN-C9**.

(*SI Appendix*, Fig. S23). The GIWAXS linecut (Fig. 3*C*) of as-cast neat **ITN-C9** films exhibits a distinct in-plane (IP) lamellar reflection (d_{100} = 19.1 Å) with a correlation length (CL) of 60.9 nm. This IP lamellar reflection is assigned to the (001) crystallographic plane, indicating that the (001) plane is perpendicular to the substrate and the **ITN-C9** molecular planes are in a "π-face-on" orientation. In addition, an out-of-plane (OOP) π–π stacking peak (d_{010} = 3.48 Å, CL = 3.1 nm) is observed, corroborating the "π-face-on" assignment. Interestingly, with annealing, the IP lamellar peak disappears and two intense OOP lamellar reflections appear (d_{100} = 13.7 and 13.1 Å) with sizeable CLs of 94.1 and 45.6 nm, respectively, consistent with a crystalline film. These OOP lamellar reflections correspond to the (011) crystallographic plane, indicating that annealing causes the crystallites to reorient such that the (011) plane becomes parallel to the substrate, resulting in a ∼65° tilt of the conjugated backbone relative to the substrate (Fig. 5*A*). In as-cast **PBDB-TF**:**ITN-C9** films, an **ITN-C9**-like OOP π–π stacking reflection (d_{010} = 3.45 Å, CL = 3.4 nm) is observed, and two IP lamellar reflections with d_{100} spacings of 21.2 (CL = 19.4 nm) and 18.6 Å (CL = 29.2 nm) are assignable to **PBDB-TF** and **ITN-C9**, respectively (Fig. 4*A* and *SI Appendix*, Table S12). Upon blend annealing, the **ITN-C9** IP lamellar reflection decreases in intensity and a new OOP lamellar reflection with d_{100} = 12.9 Å (CL = 8.2 nm) appears, suggesting that, as in the neat films, the **ITN-C9** crystallites reorient. In addition, this major morphological change agrees with the aforementioned **PBDB-TF**:**ITN-C9** film texture changes upon annealing observed in the AFM phase images. The **ITzN-C9** as-cast neat film (Fig. 3*D*) exhibits a strong OOP π–π stacking reflection (d_{010} = 3.50 Å) and a broad IP lamellar peak (d_{100} = 20.9 Å). The IP lamellar peak can be assigned to the (011) plane oriented perpendicular to the substrate surface. Both the OOP π–π stacking reflection and IP lamellar peak suggest "π-face-on" orientation. Annealing results in contraction of d_{010} to 3.42 Å coupled with an increased CL (3.4 → 4.7 nm), and an increase in intensity and CL (3.5 → 12.5 nm) of the IP lamellar peak (d_{100} contraction 20.9 → 19.3 Å), all indicating increased film crystallinity (Fig. 5*B*) compared with the as-cast film and consistent with the 10× increase in electron mobility (see *PV and Charge Transport Measurements*). Importantly, annealing does not affect **ITzN-C9** crystallite orientation, with the (011) crystallographic planes remaining perpendicular to the substrate. **ITzN-C9**:**PBDB-TF** blend films exhibit lamellar reflections in the IP and OOP directions and a strong OOP π–π stacking peak (d_{010} = 3.57 Å, CL = 2.7 nm). Interestingly, in the unannealed blends, no distinct **ITzN-C9** crystalline features are observed. However, annealing reveals obvious shoulders for the lamellar and π–π features in the IP and OOP directions, corresponding to "π-face-on" **ITzN-C9** acceptor crystallites (Fig. 4*A* and *SI Appendix*, Table S12). Overall, it can be concluded that as-cast **ITN-C9** blends form well-ordered "π-face-on" domains affording optimal PCE, while annealing causes acceptor reorientation, negatively affecting PCEs. In contrast, for **ITzN-C9**–based blends, annealing leads to acceptor crystallization with favorable "π-face-on" orientation, increasing the PCEs.

Conclusions

IT(z)N-CX, a family of π-extended IDTT-based postfullerene acceptors, is reported. Single-crystal structures of both **ITN-C9** and **ITzN-C9** reveal that the π-extended naphthyl end groups assemble in vertical columns with π-stacking distance as small as 3.31(1) Å, whereas the central IDTT cores are separated by ∼7 Å, suggesting electron transport is primarily through the LUMO-rich naphthyl end groups. These close π-stacking distances result in large electronic couplings, with a maximum value of 38 meV observed for **ITzN-C9**, which is greater than that reported for amorphous $\mathbf{PC_{61}BM}$ and $\mathbf{PC_{71}BM}$. In addition, **ITN-C9** and **ITzN-C9** have reorganization energies that are smaller than $\mathbf{PC_{61}BM}$ and $\mathbf{PC_{71}BM}$, reflecting an ability to delocalize charge over the π-system of the molecule. **ITN-C9** and **ITzN-C9** also exhibit high μ_es (10^{-4} $cm^2 \cdot V^{-1} \cdot s^{-1}$), which is likely the result of several factors, including low reorganization energies, strong multidirectional electronic couplings, and the capacity to form well-ordered crystalline domains. The solar cell performance of these acceptors was studied in blends with the **PBDB-TF** donor polymer, and optimal PCEs are achieved with as-cast **ITN-C9**–based blends, in contrast to **ITzN-C9**–based blends where annealing at the acceptor cold crystallization temperature is required. These divergent PCE outcomes can be associated with PCE-favorable "π-face-on" molecular orientation and increased crystallinity on thermal annealing for the **ITN-C9** and **ITzN-C9** blends, respectively. The results presented here provide a theoretical and experimental underpinning for the high performance observed for IDTT-based acceptors, and have implications for future nonfullerene acceptor design.

Materials and Methods

Synthesis and Characterization. **ITN-C6**, **ITN-C9**, **ITN-C12**, and **ITzN-C9** were prepared, purified, and characterized using standard synthetic techniques (*SI Appendix*, Schemes S1–S7). Crystals suitable for single-crystal X-ray diffraction were grown by diffusing acetone vapor into CH_2Br_2 solutions.

Computational Methodology. **ITIC**, **ITN**, and **ITzN** were optimized at the B3LYP/DZP level using the Amsterdam Density Functional software suite (52, 53). Alkyl chains were deleted and replaced by H atoms. Absorption spectra were obtained using ZINDO/S (54) as implemented in the ORCA software package (55) convoluted with a Gaussian profile having an SD of 0.15 eV. DOS calculations were obtained by performing a single-point calculation on the **IT(z)N-C9** crystallographic structures with the PBE functional and the Vanderbilt ultrasoft pseudopotential implemented in the Quantum Espresso plane wave software (56).

Solar Cell Fabrication. PV performance was studied using an inverted device structure, ITO/ZnO/Active layer/MoO_3/Ag. ITO substrates were washed by aqueous detergent solution, deionized water, methanol, isopropanol, and acetone (each 20 min), and cleaned by UV/ozone for 15 min. The interfacial layer ZnO was deposited from a precursor solution of 0.5 M zinc acetate dihydrate and 0.5 M ethanolamine in 2-methoxyethanol, and annealed at 170 °C for 10 min in air. The substrates were transferred into an Ar-filled glovebox for active layer spin coating. The active layer solutions were prepared by codissolving polymer and acceptors (1:1 mass ratio) in PhCl:1,8-diiodooctane (99:1 vol/vol) solvent mixture (the polymer concentration is 10 mg/mL) while stirring at 50 °C overnight. Active layers were spin-coated from the hot solution at 2,500 rpm for 60 s on a Laurell Model WS-650MZ-23NPP spin coater in the glovebox and annealed at optimized temperature and time (if needed), then dried for 1.5 h. Finally, 10 nm of MoO_3 and 100 nm of Ag were evaporated through 3 mm × 2 mm shadow mask at ∼10^{-6} Torr. No device encapsulation was used.

ACKNOWLEDGMENTS. We thank C. Stern and Dr. G. Wang for helpful discussions. This research was supported, in part, by the Argonne–Northwestern Solar Energy Research Center, an Energy Frontier Research Center funded by the US Department of Energy (DOE), Office of Science, Office of Basic Energy Sciences under Award DE-SC0001059. Research at University of Málaga was supported by Ministerio de Economia y Competitividad (Grant CTQ2015-66897-P). F.S.M. was supported by Award 70NANB14H012 from the US Department of Commerce, National Institute of Standards and Technology as part of the Center for Hierarchical Materials Design. T.J.A. and S.M.S. thank the National Science Foundation (NSF) for predoctoral fellowships. This work made use of the Electron Probe Instrumentation Center, Keck-II, and/or Scanned Probe Imaging and Development facilities of Northwestern University's Atomic and Nanoscale Characterization Experimental Center (NUANCE) which received support from the Soft and Hybrid Nanotechnology Experimental Resource (NSF Electrical, Communications, and Cyber Systems Award 1542205). Use of the Advanced Photon Source, an Office of Science User Facility operated for the US DOE Office of Science by Argonne National Laboratory, was supported by the US DOE under Contract DE-AC02-06CH11357.

1. Loo Y-L, McCulloch I (2012) Progress and challenges in commercialization of organic electronics. *MRS Bull* 33:653–662.
2. Kaltenbrunner M, et al. (2012) Ultrathin and lightweight organic solar cells with high flexibility. *Nat Commun* 3:770.
3. Mazzio KA, Luscombe CK (2015) The future of organic photovoltaics. *Chem Soc Rev* 44:78–90.
4. Lu L, et al. (2015) Recent advances in bulk heterojunction polymer solar cells. *Chem Rev* 115:12666–12731.
5. Bag S, et al. (2016) Tandem solar cells from accessible low band-gap polymers using an efficient interconnecting layer. *ACS Appl Mater Interfaces* 8:16–19.
6. Zhao W, et al. (2017) Molecular optimization enables over 13% efficiency in organic solar cells. *J Am Chem Soc* 139:7148–7151.
7. Yao K, et al. (2014) A general route to enhance polymer solar cell performance using plasmonic nanoprisms. *Adv Energy Mater* 4:1400206.
8. Savoie BM, et al. (2014) Unequal partnership: Asymmetric roles of polymeric donor and fullerene acceptor in generating free charge. *J Am Chem Soc* 136:2876–2884.
9. Cheung DL, Troisi A (2010) Theoretical study of the organic photovoltaic electron acceptor PCBM: Morphology, electronic structure, and charge localization. *J Phys Chem C* 114:20479–20488.
10. Liu T, et al. (2017) Alkyl side-chain engineering in wide-bandgap copolymers leading to power conversion efficiencies over 10. *Adv Mater* 29:1604251.
11. He Z, et al. (2015) Single-junction polymer solar cells with high efficiency and photovoltage. *Nat Photonics* 9:174.
12. Nielsen CB, Holliday S, Chen H-Y, Cryer SJ, McCulloch I (2015) Non-fullerene electron acceptors for use in organic solar cells. *Acc Chem Res* 48:2803–2812.
13. Holliday S, et al. (2015) A rhodanine flanked nonfullerene acceptor for solution-processed organic photovoltaics. *J Am Chem Soc* 137:898–904.
14. Holliday S, et al. (2016) High-efficiency and air-stable P3HT-based polymer solar cells with a new non-fullerene acceptor. *Nat Commun* 7:11585.
15. Yan C, et al. (2018) Non-fullerene acceptors for organic solar cells. *Nat Rev Mater* 3: 18003.
16. Chen W, Zhang Q (2017) Recent progress in non-fullerene small molecule acceptors in organic solar cells (OSCs). *J Mater Chem C* 5:1275–1302.
17. Meng D, et al. (2016) Three-bladed rylene propellers with three-dimensional network assembly for organic electronics. *J Am Chem Soc* 138:10184–10190.
18. Sisto TJ, et al. (2017) Long, atomically precise donor-acceptor cove-edge nanoribbons as electron acceptors. *J Am Chem Soc* 139:5648–5651.
19. Zhong Y, et al. (2014) Helical ribbons for molecular electronics. *J Am Chem Soc* 136: 8122–8130.
20. Liang N, Jiang W, Hou J, Wang Z (2017) New developments in non-fullerene small molecule acceptors for polymer solar cells. *Mater Chem Front* 1:1291–1303.
21. Lin Y, et al. (2015) An electron acceptor challenging fullerenes for efficient polymer solar cells. *Adv Mater* 27:1170–1174.
22. Zhang M, Guo X, Ma W, Ade H, Hou J (2015) A large-bandgap conjugated polymer for versatile photovoltaic applications with high performance. *Adv Mater* 27:4655–4660.
23. Li S, et al. (2017) Design of a new small-molecule electron acceptor enables efficient polymer solar cells with high fill factor. *Adv Mater* 29:1704051.
24. Li W, et al. (2018) A high-efficiency organic solar cell enabled by the strong intramolecular electron push-pull effect of the nonfullerene acceptor. *Adv Mater* 30: e1707170.
25. Han G, Guo Y, Song X, Wang Y, Yi Y (2017) Terminal [small pi]-[small pi] stacking determines three-dimensional molecular packing and isotropic charge transport in an A-[small pi]-A electron acceptor for non-fullerene organic solar cells. *J Mater Chem C* 5:4852–4857.
26. McMahon DP, Troisi A (2010) Evaluation of the external reorganization energy of polyacenes. *J Phys Chem Lett* 1:941–946.
27. Norton JE, Brédas J-L (2008) Polarization energies in oligoacene semiconductor crystals. *J Am Chem Soc* 130:12377–12384.
28. Aldrich TJ, Swick SM, Melkonyan FS, Marks TJ (2017) Enhancing indacenodithiophene acceptor crystallinity via substituent manipulation increases organic solar cell efficiency. *Chem Mater* 29:10294–10298.
29. Mei J, Bao Z (2014) Side chain engineering in solution-processable conjugated polymers. *Chem Mater* 26:604–615.
30. Huang H, Yang L, Facchetti A, Marks TJ (2017) Organic and polymeric semiconductors enhanced by noncovalent conformational locks. *Chem Rev* 117:10291–10318.
31. Jackson NE, et al. (2013) Controlling conformations of conjugated polymers and small molecules: The role of nonbonding interactions. *J Am Chem Soc* 135:10475–10483.
32. Reddy DS, Goud BS, Panneerselvam K, Desiraju GR (1993) C-H···N mediated hexagonal network in the crystal structure of the 1: 1 molecular complex 1,3,5-tricyanobenzene-hexamethylbenzene. *J Chem Soc Chem Commun* 8:663–664.
33. Bosch E, Bowling NP, Darko J (2015) The power of nonconventional phenyl C–H···N hydrogen bonds: Supportive crystal-packing force and dominant supramolecular engineering force. *Cryst Growth Des* 15:1634–1641.
34. Casalegno M, et al. (2013) Solvent-free phenyl-C61-butyric acid methyl ester (PCBM) from clathrates: Insights for organic photovoltaics from crystal structures and molecular dynamics. *Chem Commun (Camb)* 49:4525–4527.
35. Choi JH, Honda T, Seki S, Fukuzumi S (2011) Relationship between crystal packing and high electron mobility in the single crystal of thienyl-substituted methanofullerene. *Chem Commun (Camb)* 47:11213–11215.
36. Zhan XX, et al. (2016) Tailorable PC_{71} BM isomers: Using the most prevalent electron acceptor to obtain high-performance polymer solar cells. *Chemistry* 22:18709–18713.
37. Umeyama T, et al. (2017) Regioisomer effects of [70]fullerene mono-adduct acceptors in bulk heterojunction polymer solar cells. *Chem Sci (Camb)* 8:181–188.
38. Brédas J-L, Norton JE, Cornil J, Coropceanu V (2009) Molecular understanding of organic solar cells: The challenges. *Acc Chem Res* 42:1691–1699.
39. Kuzmich A, Padula D, Ma H, Troisi A (2017) Trends in the electronic and geometric structure of non-fullerene based acceptors for organic solar cells. *Energy Environ Sci* 10:395–401.
40. Coropceanu V, et al. (2007) Charge transport in organic semiconductors. *Chem Rev* 107:926–952.
41. Stehr V, Fink RF, Tafipolski M, Deibel C, Engels B (2016) Comparison of different rate constant expressions for the prediction of charge and energy transport in oligoacenes. *Wiley Interdiscip Rev Comput Mol Sci* 6:694–720.
42. Savoie BM, et al. (2014) Mesoscale molecular network formation in amorphous organic materials. *Proc Natl Acad Sci USA* 111:10055–10060.
43. Tummala NR, Zheng Z, Aziz SG, Coropceanu V, Brédas J-L (2015) Static and dynamic energetic disorders in the C60, PC61BM, C70, and PC71BM fullerenes. *J Phys Chem Lett* 6:3657–3662.
44. Troisi A (2011) Dynamic disorder in molecular semiconductors: Charge transport in two dimensions. *J Chem Phys* 134:034702.
45. Fratini S, Ciuchi S, Mayou D, de Laissardière GT, Troisi A (2017) A map of high-mobility molecular semiconductors. *Nat Mater* 16:998–1002.
46. Gajdos F, Oberhofer H, Dupuis M, Blumberger J (2013) On the inapplicability of electron-hopping models for the organic semiconductor phenyl-C61-butyric acid methyl ester (PCBM). *J Phys Chem Lett* 4:1012–1017.
47. Gajdos F, Oberhofer H, Dupuis M, Blumberger J (2014) Correction to "inapplicability of electron-hopping models for the organic semiconductor phenyl-C61-butyric acid methyl ester (PCBM)". *J Phys Chem Lett* 5:2765–2766.
48. Williams M, Tummala NR, Aziz SG, Risko C, Brédas J-L (2014) Influence of molecular shape on solid-state packing in disordered PC61BM and PC71BM fullerenes. *J Phys Chem Lett* 5:3427–3433.
49. Gali SM, Matta M, Lessard BH, Castet F, Muccioli L (2018) Ambipolarity and dimensionality of charge transport in crystalline group 14 phthalocyanines: A computational study. *J Phys Chem C* 122:2554–2563.
50. Singh TB, et al. (2007) Correlation of crystalline and structural properties of C60 thin films grown at various temperature with charge carrier mobility. *Appl Phys Lett* 90: 213512.
51. He Y, Li Y (2011) Fullerene derivative acceptors for high performance polymer solar cells. *Phys Chem Chem Phys* 13:1970–1983.
52. Kirkpatrick J (2008) An approximate method for calculating transfer integrals based on the ZINDO Hamiltonian. *Int J Quantum Chem* 108:51–56.
53. Murgatroyd PN (1970) Theory of space-charge-limited current enhanced by Frenkel effect. *J Phys D Appl Phys* 3:151–156.
54. Ridley J, Zerner M (1973) An intermediate neglect of differential overlap technique for spectroscopy: Pyrrole and the azines. *Theor Chim Acta* 32:111–134.
55. Neese F (2012) The ORCA program system. *Wiley Interdiscip Rev Comput Mol Sci* 2: 73–78.
56. Giannozzi P, et al. (2017) Advanced capabilities for materials modelling with Quantum ESPRESSO. *J Phys Condens Matter* 29:465901.
57. Kawashima K, Tamai Y, Ohkita H, Osaka I, Takimiya K (2015) High-efficiency polymer solar cells with small photon energy loss. *Nat Commun* 6:10085.